



HAL
open science

Chemical Vapor Synthesis of Zinc Oxide Nanoparticles

Nicolas Reuge, Revathi Bacsa, Philippe Serp, Brigitte Caussat

► **To cite this version:**

Nicolas Reuge, Revathi Bacsa, Philippe Serp, Brigitte Caussat. Chemical Vapor Synthesis of Zinc Oxide Nanoparticles: Experimental and Preliminary Modeling Studies. *Journal of Physical Chemistry C*, 2009, 113 (46), pp.19845-19852. 10.1021/jp9070955 . hal-03475088

HAL Id: hal-03475088

<https://hal.science/hal-03475088>

Submitted on 10 Dec 2021

HAL is a multi-disciplinary open access archive for the deposit and dissemination of scientific research documents, whether they are published or not. The documents may come from teaching and research institutions in France or abroad, or from public or private research centers.

L'archive ouverte pluridisciplinaire **HAL**, est destinée au dépôt et à la diffusion de documents scientifiques de niveau recherche, publiés ou non, émanant des établissements d'enseignement et de recherche français ou étrangers, des laboratoires publics ou privés.



Open Archive Toulouse Archive Ouverte (OATAO)

OATAO is an open access repository that collects the work of Toulouse researchers and makes it freely available over the web where possible.

This is an author -deposited version published in: <http://oatao.univ-toulouse.fr/>
Eprints ID: 3988

To link to this article: DOI:10.1021/jp9070955

URL: <http://dx.doi.org/10.1021/jp9070955>

Reuge, Nicolas and Bacsa, Revathi and Serp, Philippe and Caussat, Brigitte (2009) *Chemical Vapor Synthesis of Zinc Oxide Nanoparticles: Experimental and Preliminary Modeling Studies*. *Journal of Physical Chemistry C*, vol. 113 (n° 46). pp. 19845-19852. ISSN 1932-7447

Any correspondence concerning this service should be sent to the repository administrator:
staff-oatao@inp-toulouse.fr

Chemical Vapor Synthesis of Zinc Oxide Nanoparticles: Experimental and Preliminary Modeling Studies

Nicolas Reuge,^{*,†} Revathi Bacsa,[‡] Philippe Serp,[‡] and Brigitte Causat[†]

Laboratoire de Génie Chimique, UMR CNRS 5503, and Laboratoire de Chimie de Coordination, UPR CNRS 8241, Université de Toulouse, INPT, ENSIACET, 4, Allée Monso, BP-74233, 31432 Toulouse Cedex 4, France

The chemical vapor synthesis of ZnO tetrapods from zinc metal has been studied using a combination of experiments and fluid dynamics modeling. On one hand, an experimental study allowed production of ultrapure ZnO particles whose mean lengths (250–450 nm) and diameters (14–27 nm) depended on the reactor configuration (i.e., parallel flow/crossflow), but not on the position of air injection. On the other hand, the yield of the reaction depended both on the reactor configuration and on the position of air injection. We then developed an original kinetic model implemented in the computation fluid dynamics code FLUENT. Within the limits of certain assumptions, the model successfully predicts the experimental yield of the reaction for all the conditions tested. This good agreement shows that the kinetics of nucleation/growth of ZnO nanoparticles are probably very rapid compared to the reaction of oxidation of Zn vapor. The combination of the experimental and simulated results led to a better understanding of the heat- and mass-transfer phenomena involved. Finally, several processing parameters, such as argon and air flow rates, position of air injection, and reactor diameter, were varied in the simulations to find optimized reaction conditions for maximum yield and production rate. For the crossflow configuration, a yield of 71% and a production rate 7 times higher than the nominal value have been obtained.

1. Introduction

Because of its direct band gap (3.34 eV) and high exciton binding energy, ZnO shows high-intensity absorption for UV radiation and is therefore used as a bactericide or UV filter in medicine and cosmetics.^{1,2} High purity, controlled particle size, and ease of dispersion are the necessary criteria for these applications. Particle sizes in the range 15–50 nm are particularly interesting since they do not have the toxicity of quantum particles but at the same time they are easy to disperse and form transparent dispersions.^{3,4} Even though methods involving precipitation from the liquid phase offer good control of particle size, gas-phase synthesis techniques including aerosol and CVD are preferred for the synthesis of high-purity ZnO crystals, films, and powders.⁵ High-quality thin films of shape- and size-controlled ZnO have been produced by chemical vapor deposition (CVD) technique.^{6–8} For nanoparticle synthesis, aerosol techniques such as spray pyrolysis and chemical vapor synthesis (CVS) have been reported.⁹ CVS is a modified CVD process wherein nanoparticles produced in the gas phase are directed toward a particle collector by thermophoresis instead of forming a film.^{10–12} Recently, we reported the selective synthesis of ZnO tetrapods and spheres by CVS using zinc metal precursor for application in dye-sensitized solar cells. By simple variation of experimental conditions, it was possible to obtain nanospheres or tetrapods in the 15–50 nm size range. When applied as a photoanode in dye-sensitized solar cells, it was found that the tetrapods showed a higher efficiency of electron transfer when compared to spheres.¹³

To further improve selectivity and yield, we studied the CVS process by complementing experimental observations with a fluid dynamics model. To the best of our knowledge, no attempt has been made to model the CVS process by computational fluid dynamics (CFD). However, CFD has been used for modeling other processes such as nucleation of silicon particles from silane (SiH₄), taking into account the nucleation of Si particles in the gas phase.^{14–19} Concerning ZnO particles, only studies dealing with the mechanism of nucleation/growth are available,^{20–23} whereas the kinetics of these reactions remains unknown. It is commonly considered that ZnO is first formed through the gas-phase reaction between O₂ and Zn vapor, followed by the nucleation and growth of ZnO, leading to the formation of tetrapod whiskers.²⁰ The growth of the cylindrical arms proceeds via the nucleation of a core structure.²¹ However, the reason has not been very clear why the as-formed ZnO particles show a tetrapod structure until now.²⁰ Yu et al. revealed the presence of a tetrahedral zinc blende core from which each arm of the tetrapod grows.²² Takeuchi et al. suggest a mechanism based on multiple inversion-twin embryo.²³

In this article, we examine the influence of some key experimental parameters on the yield and production rate of ZnO tetrapods in the CVS from Zn metal precursor by using, for the first time, a combination of experiments and fluid dynamics modeling studies. In particular, the variation of the ZnO yield due to the change in reactor configuration has been examined in detail. Indeed, two configurations have been considered: the parallel flow where the reactive and carrier gases enter the reactor in the same direction and the crossflow where the directions of flow of the two gases are opposite each other. The information relative to the experimental study will be given first, followed by a description of the CFD model developed and the simulation results obtained.

* Corresponding author. Phone: 33 (0)5 34 32 36 40. Fax: 33 (0)5 34 32 37 00. E-mail: reuge@free.fr.

[†] Laboratoire de Génie Chimique, UMR CNRS 5503.

[‡] Laboratoire de Chimie de Coordination, UPR CNRS 8241.

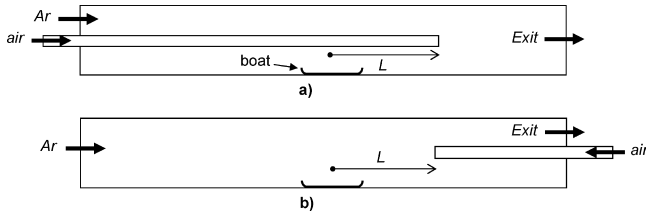


Figure 1. Schematic diagram of the experimental setup for (a) parallel flow configuration and (b) crossflow configuration.

2. Experimental Investigations

2.1. Process Description and Operating Conditions. A schematic diagram of the experimental setup is shown in Figure 1. The synthesis was carried out in a horizontal 110-cm long and 2.6-cm diameter tubular quartz reactor. The central part (61-cm length) of the reactor was enclosed in a tubular furnace whose temperature was set at 900 °C. A three-zones furnace was used to achieve a sufficiently long isothermal zone. Zinc metal powder (0.5 g) contained in an alumina boat was introduced into the central hot zone under an argon atmosphere. Zn vapor was oxidized by a flux of dry air brought into the hot zone of the reactor by a smaller tube (5-mm inner diameter; 8-mm outer diameter). Two configurations were studied, depending on the direction of the air flux: parallel flow (Figure 1a) and crossflow (Figure 1b). The axial distance L between the center of the boat and the point of air injection was a modifiable parameter (Figure 1).

All experiments were carried out under atmospheric pressure. The flow rates of argon and air were 2×10^{-5} and 3.06×10^{-5} $\text{m}^3 \cdot \text{s}^{-1}$ STP respectively. Several values for L have been tested. For parallel flow, the values of L were -4 , 0 , 4 , 8 , 12 , 16 , and 20 cm. For crossflow, the L values were 15 , 20 , 25 , and 30 cm. The actual temperature along the reactor wall was measured for both configurations and for all values of L under gas flow. Changing L leaves the temperature profile of the reactor unchanged. Moreover, the temperature profiles for the parallel flow and the crossflow configurations were found to be nearly the same. Inside the heated zone, the temperature remained at 900 °C over a length of about 30 cm. The oxidation of Zn vapor gave rise to thick white fumes that turned to fluffy white flakes transported toward the cold end of the reactor. They were collected by cold traps and weighed. The mass of this ZnO was called $m_{\text{ZnO}}^{\text{out}}$. This weight also included the part of ZnO deposited on the cold part of the reactor since it was collected a posteriori and put together with those collected in the cold traps. We feel that the ZnO deposited on the cold walls immediately before the cold traps is indeed part of the yield and the deposition could

have been avoided if the reactor tube had been shorter/more efficiently cooled at the reactor exit. All structural investigations point out that ZnO collected in this part resembles that collected in the cold traps.

The ZnO deposited on the hot walls of the reactor was collected after the reactor was cooled down in air. This fraction was named $m_{\text{ZnO}}^{\text{wall}}$. For some runs, a significant part of the Zn powder did not evaporate but was oxidized directly into the boat; this part of ZnO collected into the boat was called $m_{\text{ZnO}}^{\text{boat}}$. A summary of the different experimental conditions studied and the corresponding masses of ZnO obtained in the different zones are presented in Table 1.

The crystal structure and microstructure of the powders were determined using X-ray crystallography and scanning electron microscopy (Seifert C 3000 Powder X-ray diffractometer and Field Effect Gun SEM JEOL 6700F). BET surface areas of the powders were calculated by measuring nitrogen adsorption at liquid nitrogen temperature (Belsorp-mini).

2.2. Results and Discussion. 2.2.1. Reaction Yields. The reaction was complete in about 3 min 30 s for all runs except runs 1 and 8 that lasted over 4 min. Some ZnO was collected into the boat only for runs 1 and 8; for the other runs, neither Zn nor ZnO was present in the boat, showing the total evaporation of zinc under the experimental conditions employed. The powders synthesized are white for all runs except for runs 7 and 11 for which the powders collected are gray, revealing an incomplete oxidation of Zn. The complete oxidation of 0.5 g of Zn leads to 0.625 g of ZnO. However, the sum of the collected masses of ZnO ($m_{\text{ZnO}}^{\text{out}} + m_{\text{ZnO}}^{\text{wall}} + m_{\text{ZnO}}^{\text{boat}}$) after experiments is lower than this value for all runs. As reported in Table 1, the uncollected mass varies between 11% and 20% depending on the experimental conditions. The uncollected mass remained the same even if higher quantities of Zn were sublimed. Hence, it is deduced that this error is probably due to incomplete recovery of ZnO in the aerosol or from the walls of the reactor. For larger scale production, this error is expected to be negligible.

The experimental yield is calculated using the following expression:

$$Y = \frac{m_{\text{ZnO}}^{\text{out}}}{m_{\text{ZnO}}^{\text{out}} + m_{\text{ZnO}}^{\text{wall}} + m_{\text{ZnO}}^{\text{boat}}} \quad (1)$$

The values obtained using eq 1 are reported in Table 1 for the different experimental conditions employed. In the case of the parallel flow configuration, the yield increases when L is increased from -4 to 12 cm and decreases for higher values of L . The maximum yield (for $L = 12$ cm) is 46.8%. For crossflow configuration, a similar trend is observed with a maximum yield

TABLE 1: Summary of the Experimental Conditions Including Experimental and Calculated Yields for the Synthesis of ZnO in the Parallel Flow and Crossflow Configurations

| run/configuration | L (cm) | $m_{\text{ZnO}}^{\text{out}}$ (g) | $m_{\text{ZnO}}^{\text{wall}}$ (g) | $m_{\text{ZnO}}^{\text{boat}}$ (g) | uncollected mass (g, %) | experimental yield (%) | calculated yield (%) |
|-------------------|----------|-----------------------------------|------------------------------------|------------------------------------|-------------------------|------------------------|----------------------|
| 1/parallel flow | -4 | 0.084 | 0.058 | 0.359 | 0.124,19.8 | 16.8 | 7 |
| 2/parallel flow | 0 | 0.144 | 0.376 | 0 | 0.105,16.8 | 27.7 | 24 |
| 3/parallel flow | 4 | 0.150 | 0.337 | 0 | 0.138,22.1 | 30.8 | 30.8 |
| 4/parallel flow | 8 | 0.172 | 0.340 | 0 | 0.113,18.1 | 33.6 | 38.2 |
| 5/parallel flow | 12 | 0.195 | 0.300 | 0 | 0.13,20.8 | 39.4 | 46.8 |
| 6/parallel flow | 16 | 0.197 | 0.346 | 0 | 0.082,13.1 | 36.3 | 42.6 |
| 7/parallel flow | 20 | 0.195 ^a | 0.320 | 0 | 0.11,17.6 | | |
| 8/crossflow | 15 | 0.194 | 0.122 | 0.218 | 0.091,14.6 | 36.3 | 26.7 |
| 9/crossflow | 20 | 0.322 | 0.232 | 0 | 0.071,11.4 | 58.1 | 58.1 |
| 10/crossflow | 25 | 0.335 | 0.22 | 0 | 0.07,11.2 | 60.4 | 59.1 |
| 11/crossflow | 30 | 0.372 ^a | 0.153 | 0 | 0.1,1.6 | | |

^a Presence of unoxidized Zn in the powder.

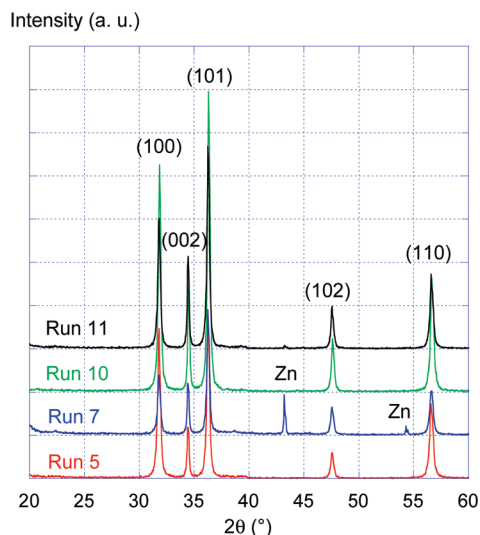


Figure 2. X-ray diffractograms of ZnO powders obtained using the parallel flow and crossflow configurations.

of 59.1% for $L = 25$ cm. Hence, the crossflow configuration appears to be more efficient in terms of yield. Reruns performed to confirm this trend showed similar results (differences in the yield not greater than 1%) and hence the reproducibility of these results is very good.

2.2.2. Characterization. Figure 2 shows the X-ray diffractograms of ZnO powders obtained using the parallel flow and crossflow configurations. For all runs except those using very large values of L , ZnO wurtzite (JCPDS 36-1451) is the only crystalline phase obtained. For large values of L , in both configurations (run 7 with $L = +20$ cm for parallel flow and run 11 for crossflow with $L = 30$ cm), reflections due to Zn metal are observed showing incomplete oxidation, probably because of the lower concentration of oxygen for these values of L . This effect is more pronounced for the parallel flow configuration than for the crossflow configuration. An influence of oxygen content on the structure of ZnO produced by CVS was reported earlier.¹² Measurements of intensities of the reflections from the different crystallographic planes showed that in certain cases, for example, for run 5, a higher intensity (20% increase) has been observed for the (100) reflection when compared to that of standard ZnO (JCPDS 36-1451), showing preferential crystal growth. However, a systematic variation has not been observed as a function of L . This result is in contrast to the complete disappearance of a crystal plane (002) in the presence of dopants such as indium during the synthesis of ZnO nanorods by flame spray pyrolysis.²⁴

Figure 3 shows representative scanning electron microscopy (SEM) images of ZnO tetrapods produced by CVS in parallel flow ($L = +4$ cm) and crossflow ($L = 20$ cm) conditions, respectively. It is seen that most of the particles have tetrapod shapes formed by the assembly of four nanorods, details of which are reported in a previous publication.¹³ The SEM images for runs 7 and 11 (not shown) did not show any significant change in morphology of ZnO because of incomplete oxidation but showed cubic particles of a second phase, that of zinc metal as seen in the XRD. Thus, the lower oxygen concentration has only a limited influence on morphology of ZnO at 900 °C.

The length and diameter distributions of the tetrapods vary only slightly with the values of L but change significantly if the reactor configuration is modified. The mean length and diameter of the rods forming the tetrapods have been calculated from the analysis of a number of images from both configura-

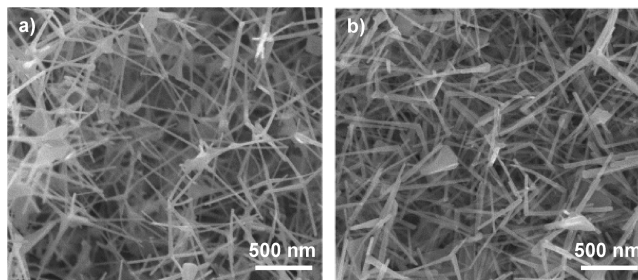


Figure 3. SEM images of ZnO nanoparticles obtained from (a) run 11 (parallel flow) and (b) run 9 (crossflow).

tions, totaling up to 860 measurements. The results are reported in Table 2 and in Figure 4. It is seen that the parallel flow configuration results in long fine rods with mean diameter of 17 nm and lengths varying from 100 to 900 nm (Figure 4a), giving a maximum aspect ratio of 50. Over 10% of the rods measured have less than 10-nm diameter (Figure 4b). However, ZnO tetrapods produced by crossflow have a higher diameter (less than 5% have a diameter less than 15 nm) (Figure 4b) and are shorter (average length of 266 nm) (Figure 4a). It follows that the mean nanorods volume is higher for the crossflow product when compared to that of the parallel flow product by a factor of 1.6. In other words, particles synthesized in crossflow are more compact and massive than the ones formed in parallel flow. The parallel flow also produces tetrapods with a much narrower diameter distribution than the crossflow configuration. These results have been confirmed by a higher BET surface area ($22 \text{ m}^2 \cdot \text{g}^{-1}$) for the parallel flow configuration when compared to that prepared using crossflow ($16 \text{ m}^2 \cdot \text{g}^{-1}$).

3. CFD Modeling of the Process

3.1. General Model Features. The CFD code FLUENT (version 6.3.26) was used for this study. The governing equations used for the model, i.e., the continuity equation, the Navier–Stokes equation, the energy equation, and the species mass conservation equations, can be found in the FLUENT User Guide.²⁵ The set of these nonlinear equations was linearized using the SIMPLE algorithm and the order 1 was chosen for spatial discretization. Under the chosen experimental parameters, it was possible to safely assume laminar flow. Gases were considered to be perfect and steady-state conditions were assumed. Conduction of heat in the inner smaller diameter tube wall was taken into account. The species considered were Ar, N_2 , O_2 , Zn, and ZnO. It was assumed that all of them remained as gases in the homogeneous phase. In other words, the nucleation process of Zn and ZnO was ignored. This is a strong but unavoidable assumption for the feasibility of the model since the kinetics of the nucleation/growth are unknown. Species mass transfer was therefore assumed to result only from ordinary diffusion and convection. ZnO particles thermophoresis,^{26–28} which could exist in this process, has been neglected.

The exact form of the multicomponent diffusion was considered to describe the diffusive transport of these gaseous species.²⁵ The binary diffusion coefficients were calculated using the kinetic theory:²⁵ the Lennard-Jones parameters of gaseous Zn were found in the literature²⁹ and the same coefficients were used for ZnO. The quartz reactor was considered in its entirety for the simulations, i.e., the heated zone of 61 cm and the extensions on both sides (25 cm on each side). Except for the boat, the geometry of the reactor is axisymmetric. For the simulations, both 2-D axisymmetric and 3-D approaches were tested. The grid sizes for the 2-D and 3-D simulations were

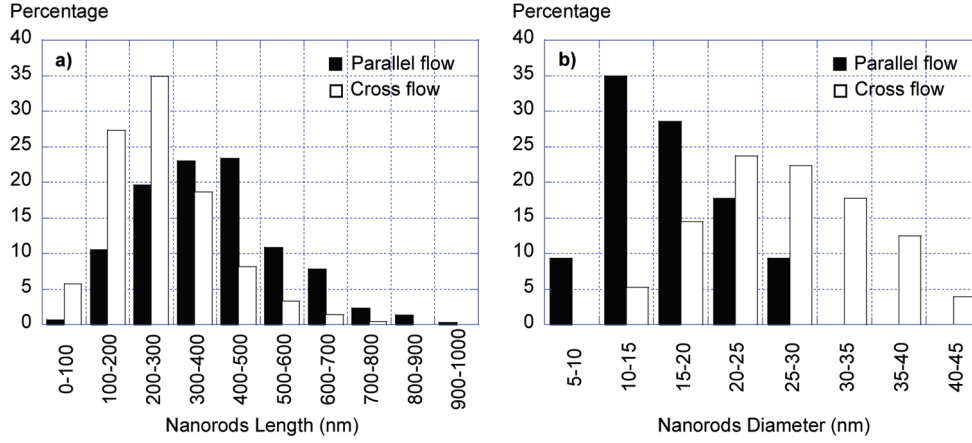


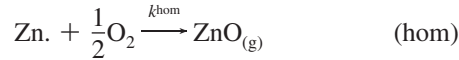
Figure 4. Histograms of distributions of (a) nanorods length and (b) nanorods diameter for the tetrapods synthesized using the parallel flow and crossflow configurations.

TABLE 2: Diameter and Length Measurements Made from SEM Images for ZnO Tetrapods Synthesized Using the Parallel Flow and Crossflow Configurations

| run/configuration | nanorods mean length (nm) | standard deviation (nm) | nanorods mean diameter (nm) | standard deviation (nm) |
|------------------------|---------------------------|-------------------------|-----------------------------|-------------------------|
| 1/parallel flow | 404 | 185 | 19 | 5 |
| 2/parallel flow | 418 | 155 | 18 | 6 |
| 3/parallel flow | 420 | 166 | 14 | 5 |
| 5/parallel flow | 405 | 164 | 16 | 5 |
| 9/crossflow | 250 | 124 | 27 | 8 |
| 10/crossflow | 283 | 130 | 27 | 8 |
| mean for parallel flow | 412 | 167 | 17 | 5 |
| mean for crossflow | 266 | 127 | 27 | 8 |

18970 cells and 508300 cells, respectively. Grid independence of the results was verified.

3.2. Chemical Model and Kinetics. In the gas phase, Zn vapor is oxidized according to the following homogeneous reaction:³⁰

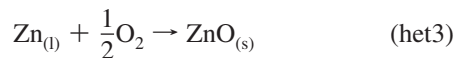


Following this reaction, gaseous ZnO condenses very quickly to form nanoparticles of solid ZnO.^{20,30} To explain the formation of ZnO on the reactor wall, two possible mechanisms have been envisaged:

- (1) The direct deposition of ZnO formed in the gaseous phase:



- (2) The condensation of Zn vapor, followed by oxidation:



From Garcia et al.,³¹ the activation energy of the reaction (hom) is 129 kJ·mol⁻¹. To the best of our knowledge, the pre-exponential factor k_0^{hom} is unknown. Considering the heat of formation of the species involved and from Müller et al.,³² its enthalpy is 470 kJ·mol⁻¹. Hence, this reaction is strongly exothermic. For the reaction (het1), a mechanism of physisorption/condensation with activation energy of 0 has been consid-

ered. The pre-exponential factor k_0^{het1} is also unknown. The reaction of Zn recondensation (het2) cannot occur while the wall temperature remains equal to the temperature of Zn evaporation, i.e., 900 °C. So (het2) becomes active wherever the wall temperature is lower. It is important to note that Zn vapor condenses as liquid Zn as long as the wall temperature is higher than 420 °C (i.e., the melting point of Zn). For wall temperatures below 900 °C, Zn vapor, which is a radical species, is assumed to deposit on the walls with a sticking coefficient of 1. This leads to the following kinetics:

$$k^{\text{het2}} = 9\sqrt{T} \quad (2)$$

Calculations will show that this reaction occurs in zones that are poor in oxygen and therefore the subsequent oxidation reaction (het3) can be ignored (the complete oxidation of deposited Zn may occur after the experiment when the reactor is open).

3.3. Processing Parameters, Boundary Conditions, and Yield. All the processing parameters used for the simulations have been detailed in section 2. The temperature profiles measured along the reactor wall have been applied as boundary conditions (BC) in the simulations. Experimental evaporation rates of Zn (i.e., 0.5 mg·s⁻¹ for run 1, 1.1 mg·s⁻¹ for run 8, and 2.4 mg·s⁻¹ for the other runs) have been applied as wall BC at the location of the boat.

From the simulation results, the yield was calculated as follows:

$$Y = \frac{F_{\text{ZnO}}^{\text{out}}}{F_{\text{ZnO}}^{\text{out}} + F_{\text{ZnO}}^{\text{wall}} + 1.25 \cdot F_{\text{Zn}}^{\text{wall}} + G_{\text{ZnO}}^{\text{boat}}} \quad (3)$$

where $F_{\text{ZnO}}^{\text{out}}$ is the mass flow rate of ZnO exiting the reactor, $F_{\text{ZnO}}^{\text{wall}}$ and $F_{\text{Zn}}^{\text{wall}}$ are respectively the mass flow rates of ZnO and

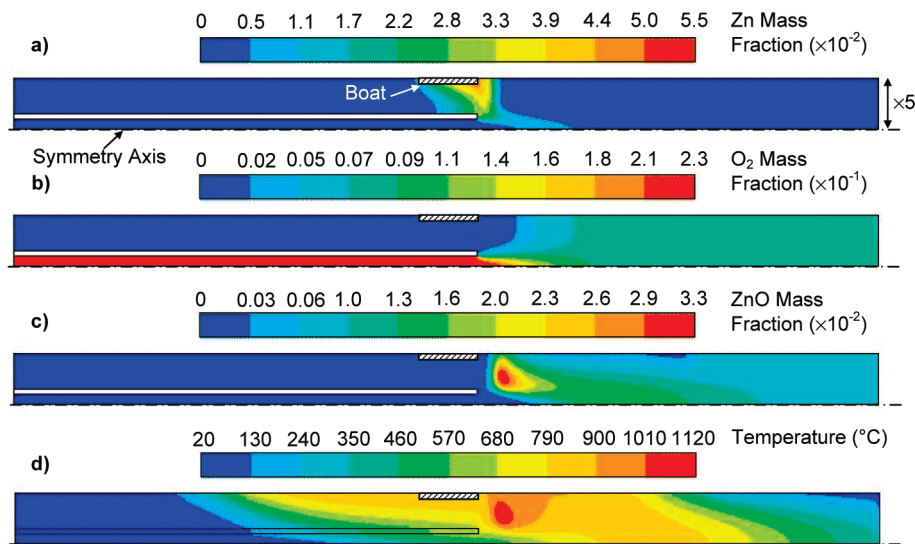


Figure 5. Fields of (a) Zn mass fraction, (b) O₂ mass fraction, (c) ZnO mass fraction, and (d) temperature, calculated for run 3 (parallel flow, $L = +4$ cm).

Zn depositing on the reactor wall in the heated zone (note that $F_{Zn}^{y,all}$ is multiplied by 1.25 to consider the subsequent oxidation of Zn deposited), and G_{ZnO}^{boat} is the experimental formation rate of ZnO into the boat (1.4 $mg \cdot s^{-1}$ for run 1, 0.84 $mg \cdot s^{-1}$ for run 8, and 0 for the other runs). Note that expressions (1) and (3) are equivalent.

3.4. Adjustment of Kinetics and Comparison of 2-D/3-D Calculations. 2-D axisymmetric calculations were performed to estimate the values of the missing kinetic parameters. The pre-exponential factor k_0^{hom} has been adjusted for the parallel flow configuration in such a way that the oxidation of Zn vapor is complete for all runs except run 7. This leads to a value of k_0^{hom} of $8 \times 10^8 m^{3/2} \cdot mol^{-1/2} \cdot s^{-1}$. This value of k_0^{hom} has been used for the crossflow configuration: complete oxidation of Zn was obtained for all runs except run 11 as observed in the experimental runs.

Similarly, the pre-exponential factor k_0^{het1} has first been adjusted in such a way that the calculated yield is equal to the experimental yield for run 3 (parallel flow, $L = +4$ cm, yield of 30.8%). This leads to a value of k_0^{het1} of $0.07 m \cdot s^{-1}$. However, when k_0^{het1} from run 9 is adjusted (crossflow, $L = 20$ cm, yield of 58.1%), a value of $0.007 m \cdot s^{-1}$ is obtained. This difference (of a factor 10) might be explained by the different particle morphologies obtained in the two configurations. However, this aspect cannot be verified since the kinetics of nucleation of Zn and ZnO are unknown. These two values of k_0^{het1} have been validated by comparison of the calculated yields with the experimental yields obtained for the other runs for each configuration, as described below in section 3.5.2.

Subsequently, 3-D calculations were performed for runs 3 and 9 with the previously adjusted values for the kinetic parameters, and yields were calculated. This leads to yields of only 4–5% higher than the ones obtained with the 2-D calculations. These weak differences can be explained by the fact that the radial diffusion of Zn vapor and ZnO across the reactor is rapid compared to axial convection. Therefore, it can be concluded that performing calculations in 3-D is not necessary despite the non-axisymmetry of the boat. All subsequent calculations have been performed with a 2-D axisymmetric approach.

3.5. Results and Discussion. 3.5.1. Mass Fractions and Temperature Profiles. Figure 5 presents the Zn mass fraction

field (Figure 5a), the O₂ mass fraction field (Figure 5b), the ZnO mass fraction field (Figure 5c), and the temperature field (Figure 5d) calculated for run 3 (parallel flow, $L = 4$ cm). Figure 5a,b shows that the mixing between Zn and O₂ begins a few centimeters away from the boat. Following this, the production of ZnO occurs as shown in Figure 5c. The increase in temperature to 995 °C (see Figure 5d) in this zone of oxidation is due to the strong exothermic nature of the reaction (hom). The depletion of ZnO mass fraction near the reactor wall is due to the deposition reaction (het1).

We now compare this result with the ZnO mass fraction field obtained for $L = -4$ cm in the same configuration (Figure 6a). This figure shows that most ZnO is produced in the region directly above the boat. Actually, for this case, oxygen diffuses to the boat. This is why a part of Zn is oxidized directly into the boat as observed experimentally.

Figure 7 shows the Zn mass fraction field (Figure 7a), the O₂ mass fraction field (Figure 7b), the ZnO mass fraction field (Figure 7c), and the temperature field (Figure 7d) calculated for run 7 (crossflow, $L = 20$ cm). Figure 7a,b shows that the mixing between Zn and O₂ begins a few centimeters after the boat. Then the production of ZnO occurs as shown in Figure 7c. The temperature increases to 970 °C (see Figure 6d) in this zone of oxidation.

Figure 6b presents the ZnO mass fraction field for run 8 (crossflow, $L = 15$ cm). As for run 1, ZnO is produced just over the boat. Oxygen diffusing to the boat, the fact that a part of Zn is oxidized directly into the boat, appears logical once again.

For run 3 (parallel flow configuration/ $L = +4$ cm), the radial temperature gradient predicted by the model close to the wall is about 43 °C/mm in the zone of production of ZnO and 37 °C/mm at the end of the heated zone. For run 7 (crossflow configuration/ $L = 20$ cm), they are 59 and 27 °C/mm, respectively. A significant contribution of the thermophoresis in the deposition of ZnO tetrapods is therefore probable. Neglecting the thermophoresis results in the obtention of apparent pre-exponential factors k_0^{het1} that do not have a strictly chemical nature, but it is usual to proceed as this in a first approach for the modeling of CVD processes that are too complex to be completely represented by a model.^{33,34} However, even if the ZnO walls deposition is mainly due to thermophore-

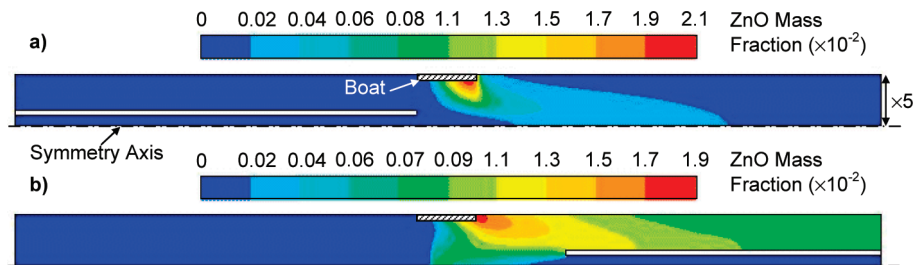


Figure 6. Fields of ZnO mass fraction calculated for (a) run 1 and (b) run 8.

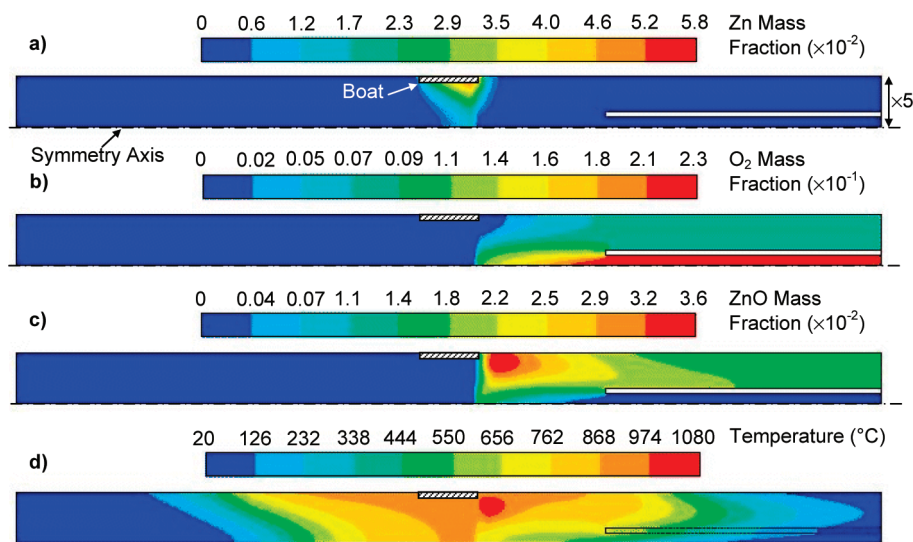


Figure 7. Fields of (a) Zn mass fraction, (b) O₂ mass fraction, (c) ZnO mass fraction, and (d) temperature, calculated for run 7 (crossflow, $L = 20$ cm).

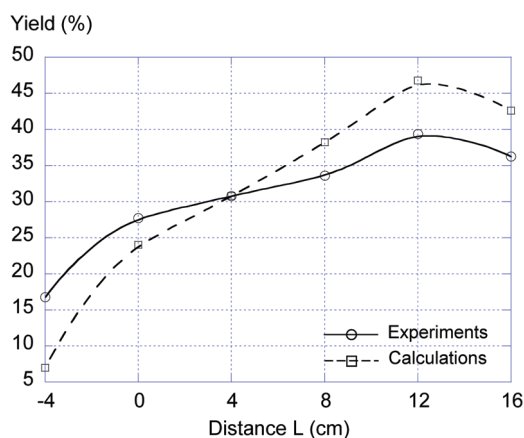


Figure 8. Experimental and calculated yield vs distance L for the parallel flow configuration.

sis and not to ordinary diffusion, the temperature gradients aforementioned being of the same order of magnitude, this cannot explain the difference of a factor of 10 found for k_0^{het1} between the two configurations.

According to the model, the temperature in the zone of ZnO production for the parallel flow configuration is about 100 °C higher than the temperature in the zone of ZnO production for the crossflow configuration. The reason is that the zone of production of ZnO is more concentrated for the parallel flow configuration and the heat produced by the oxidation reaction is more localized. We think that this point could explain the different nanorods diameters and lengths and then the factor of 10 found for k_0^{het1} between the two configurations.

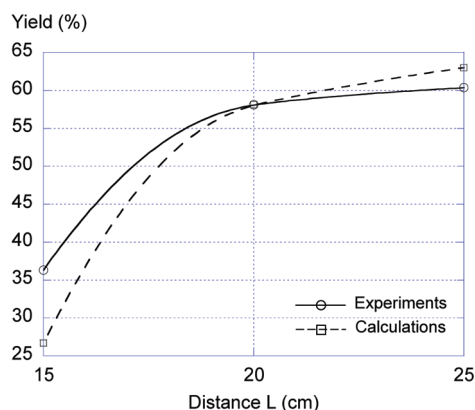


Figure 9. Experimental and calculated yield vs distance L for the crossflow configuration.

3.5.2. Reaction Yield. The yields obtained from the simulations are given in Table 1. Figures 8 and 9 present the experimental and the calculated yields as a function of L for the parallel flow and crossflow configurations, respectively. It appears that the experimental trends are well reproduced by calculations. This tends to demonstrate the validity of our chemical and kinetic models. In particular, the kinetics of nucleation/growth of ZnO nanoparticles are probably very rapid compared to the reaction of oxidation of Zn vapor and then are not a limiting step in this process.

For the parallel flow configuration, the calculated yields are overestimated for $L > 4$ cm and underestimated for $L < 4$ cm. The increase of the yield from $L = -4$ cm to $L = +12$ cm can now be explained: after the conversion of Zn into ZnO, the

TABLE 3: Simulations of Optimization: Processing Parameters and Results

| run/configuration | D (cm) | L (cm) | Q_{Ar}^* | Q_{air}^* | calculated yield (%) | normalized ZnO production |
|------------------------|------------|-----------|-------------------|--------------------|----------------------|---------------------------|
| 5/parallel flow | 2.6 | 12 | 1 | 1 | 46.3 | 1 |
| S1/parallel flow | 2.6 | 8 | 1 | 1.5 | 45.9 | 0.99 |
| S2/parallel flow | 2.6 | 16 | 1 | 0.66 | 33 | 0.71 |
| S3/parallel flow | 2.6 | 12 | 2 | 1 | 48.8 | 2.11 |
| S4/parallel flow | 2.6 | 12 | 2.4 | 1 | 51.3 | 2.64 |
| S5/parallel flow | 4 | 12 | 3.3 | 1 | 57.5 | 4.1 |
| S6/parallel flow | 4 | 12 | 4 | 1 | 60.3 | 5.21 |
| S7/parallel flow | 6 | 12 | 5 | 1 | 59.6 | 6.43 |
| 10/crossflow | 2.6 | 25 | 1 | 1 | 63 | 1.36 |
| S8/crossflow | 4 | 25 | 2.4 | 1 | 72.8 | 3.77 |
| S9/crossflow | 4 | 25 | 3 | 1 | 67.8 | 4.39 |
| S10/crossflow | 6 | 20 | 5 | 1 | 71 | 7.66 |

shorter the distance for the gaseous mixture to exit the heated zone (i.e., the longer is L), the shorter the time for ZnO to deposit on the walls. The decrease of the yield for $L < 12$ cm can also be clarified: unoxidized Zn vapor may be present at the point where the gaseous mixture leaves the isothermal zone (900 °C). Hence, (het2) becomes active; unoxidized zinc condenses on the reactor wall.

For the crossflow configuration, the calculated yields are overestimated for $L > 20$ cm and underestimated for $L < 20$ cm. The increase of the yield with L can be explained in the same manner as for the parallel flow configuration.

3.5.3. Optimization of Reaction Conditions for Maximum Yield and Production Rate. The experimental results and calculations in the previous sections have shown that the yield can be optimized by adjusting the distance L . Additional calculations have then been carried out to optimize the process in terms of yield and production rate of ZnO for the two configurations, varying argon and air flow rates and the reactor diameter. Results are reported in Table 3, where D is the reactor diameter and Q_{Ar}^* and Q_{air}^* are the flow rates of argon and air normalized as a function of the flow rates previously used. The ZnO production has been normalized as a function of the production of run 8 (parallel flow, $L = +12$ cm). Note that the flux of evaporating Zn has been assumed proportional to the argon flow rate.

In the parallel flow configuration (S1–S7), simulation S1 shows that an increase in air flow rate does not allow a better yield to be obtained, compared to run 5. (Several L values have been tested, we present only the case with $L = +12$ cm for which the yield is maximum.) Simulation S2 shows that a decrease in air flow rate results in a significantly lower yield. (L has been increased to +16 cm to maximize the yield.) In contrast, simulations S3 and S4 show that an increase in argon flow rate tends to increase slightly the yield. This can be explained by the shorter residence time of ZnO in the heated zone. Moreover, increasing the argon flow rate is obviously very beneficial in terms of ZnO production rate. With $L = +12$ cm, the maximum value for Q_{Ar}^* to ensure a complete oxidation is 2.4 (run S4). Simulations S5 and S6 show that an increase in reactor diameter to 4 cm (and then to a lower S/V ratio) allows the yield (up to 60.3%, run S6), the argon flow rate, and therefore the production rate of ZnO to increase. With this reactor diameter and with $L = +12$ cm, the maximum value for Q_{Ar}^* is 4 (run S6). With a reactor diameter of 6 cm, Q_{Ar}^* can be increased to 5 (run S7). For these conditions, the oxygen flux is almost completely consumed by the oxidation reaction (hom). Run S7 yields the best normalized production rate in parallel flow with a value of 6.43. The yield of run S7 is slightly lower than that of run S6 because of the recondensation of a part of Zn vapor on the reactor wall.

For the simulations S8–S10, the configuration is crossflow. With a reactor diameter of 4 cm, L of 25 cm, and Q_{Ar}^* of 2.4, simulation S8 shows that the yield (72.8%) and the ZnO production rate are significantly increased compared to those of run 10. With Q_{Ar}^* of 3 (run S9), the production is still increased but the yield is lower than the one obtained with run S8 because of recondensation of Zn vapor. With a reactor diameter of 6 cm, L of 20 cm, and Q_{Ar}^* of 5 (run S10, L had to be decreased to 20 cm to ensure a complete oxidation of Zn), the yield is good (71%) and the normalized production reaches 7.66, which is a huge improvement.

Therefore, this optimization study shows that each tested parameter (D , L , Q_{Ar}^* , and Q_{air}^*) has an effect on the yield and the production rate of ZnO. These effects are not always predictable because of the numerous physicochemical phenomena that interact. It would be laborious to test all the different combinations. However, these simulations highlight the ways of how the CVS process can be optimized in terms of yield and production rate.

4. Conclusion

We have used a combination of experiments and fluid dynamics modeling to study the effect of some key operating parameters on the yield and production rate in the chemical vapor synthesis of ZnO tetrapods.

First, an experimental study allowed production of ZnO particles with high purity. Mean lengths (250–450 nm) and diameters (14–27 nm) of the nanorods were revealed to depend on the reactor configuration (i.e., parallel flow/crossflow), but not on the position of air injection. For the crossflow configuration, the synthesized nanorods were more compact and massive than those for the parallel flow configuration. The yield of the reaction depended both on the reactor configuration and on the position of air injection. It was maximum for the crossflow configuration.

We then developed an original kinetic model for this CVS process, and we implemented it in the computation fluid dynamics code FLUENT. Within the limits of certain assumptions, the model successfully predicts the experimental yield of the reaction for all the conditions tested. This good agreement shows that the kinetics of nucleation/growth of ZnO nanoparticles are probably very rapid compared to the reaction of oxidation of Zn vapor. The combination of the experimental and simulated results leads to a better understanding of the heat- and mass-transfer phenomena involved. In addition, this approach has resulted in improvement in the yield and selectivity for both parallel flow and crossflow configurations.

Finally, several processing parameters, such as argon and air flow rates, position of air injection, and reactor diameter, were

varied in the simulations to find optimized reaction conditions for maximum yield and production rate. For the crossflow configuration, a yield of 71% and a production rate 7 times higher than the nominal value have been obtained. Hence, such an approach is expected to help development of large-scale production of nanocrystalline ZnO.

Acknowledgment. The authors thank D. Neumeyer for the measurement of BET surface area and X-ray diffractograms and S. Le blond du Plouy (TEMSCAN, Toulouse University) for the SEM images. Research funding from Agence Nationale de Recherche, France (RNMP05-PRONANOX), and Midi Pyrénées Regional council are gratefully acknowledged.

References and Notes

- (1) Schmidt-Mende, L.; MacManus-Driscoll, J. L. *Mater. Today* **2007**, *10*, 40.
- (2) Pinnell, S. R.; Fairhurst, D.; Gillies, R.; Mitchnick, M. A.; Kollias, N. *Dermatol. Surg.* **2000**, *26*, 309.
- (3) Serpone, N.; Dondi, D.; Albin, A. *Inorg. Chim. Acta* **2007**, *360*, 794.
- (4) Dodd, A. C.; McKinley, A. J.; Saunders, M.; Tsuzuki, T. *J. Nanopart. Res.* **2006**, *8*, 43.
- (5) Tani, T.; Mädler, L.; Pratsinis, S. E. *J. Nanopart. Res.* **2002**, *4*, 337.
- (6) Ye, C.; Fang, X.; Hao, Y.; Teng, X.; Zhang, L. *J. Phys. Chem. B* **2005**, *109*, 19758.
- (7) Wang, Z. L. *J. Phys.: Condens. Matter* **2004**, *16*, R829.
- (8) Özgür, Ü; Alivov, Y. I.; Liu, C.; Teke, A.; Reshchikov, M. A.; Doğan, S.; Avrutin, V.; Cho, S.-J.; Morkoç, H. *J. Appl. Phys.* **2005**, *98*, 041301.
- (9) Klein, S.; Winterer, M.; Hahn, H. *Chem. Vap. Deposition* **1998**, *4*, 143.
- (10) Polarz, S.; Roy, A.; Merz, M.; Halm, S.; Schroder, D.; Schneider, L.; Bacher, G.; Kruis, F. E.; Driess, M. *Small* **2005**, *1*, 540.
- (11) Jin, W.; Lee, I.-K.; Kompch, A.; Dörfler, U.; Winterer, M. *J. Eur. Ceram. Soc.* **2007**, *27*, 4333.
- (12) Bacsa, R.; Kihn, Y.; Verelst, M.; Dexpert, J.; Bacsa, W.; Serp, P. *Surf. Coat. Technol.* **2007**, *201*, 9200.
- (13) Bacsa, R. R.; Dexpert-Ghys, J.; Verelst, M.; Falqui, A.; Machado, B.; Bacsa, W. S.; Chen, P.; Zakeeruddin, S. M.; Graetzel, M.; Serp, P. *Adv. Funct. Mater.* **2009**, *19*, 875.
- (14) Vorob'ev, A. N.; Komissarov, A. E.; Segal, A. S.; Makarov, Y. N.; Karpov, S. Y.; Zhmakin, A. I.; Rupp, R. *Mater. Sci. Eng., B* **1999**, *61–62*, 176.
- (15) Vorob'ev, A. N.; Karpov, S. Y.; Bord, O. V.; Zhmakin, A. I.; Lovtsus, A. A.; Makarov, Y. N. *Diamond Relat. Mater.* **2000**, *9*, 472.
- (16) Vorob'ev, A. N.; Karpov, S. Y.; Zhmakin, A. I.; Lovtsus, A. A.; Makarov, Y. N.; Krishnan, A. *J. Cryst. Growth* **2000**, *211*, 343.
- (17) Kremer, D. M.; Davis, R. W.; Moore, E. F.; Ehrman, S. H. *J. Cryst. Growth* **2003**, *247*, 333.
- (18) Kremer, D. M.; Davis, R. W.; Moore, E. F.; Ehrman, S. H. *Chem. Eng. Sci.* **2004**, *59*, 1115.
- (19) Nijhawan, S.; McMurry, P. H.; Swihart, M. T.; Suh, S.-M.; Girshick, S. L.; Campbell, S. A.; Brockmann, J. E. *Aerosol Sci.* **2003**, *34*, 691.
- (20) Hwang, C.-C.; Lin, C.-S.; Wang, G.-P.; Peng, C.-H.; Chung, S.-L. *J. Alloys Compd.* **2009**, *467*, 514.
- (21) Newton, M. C.; Warburton, P. A. *Mater. Today* **2007**, *10*, 50.
- (22) Yu, W. D.; Li, X. M.; Gao, X. D. *Chem. Phys. Lett.* **2004**, *390*, 296.
- (23) Takeuchi, S.; Iwanaga, H.; Fuji, M. *Philos. Mag. A* **1994**, *69*, 1125.
- (24) Height, M.; Mädler, L.; Pratsinis, S. E. *Chem. Mater.* **2005**, *18*, 572.
- (25) *FLUENT User Guide*; Fluent Inc.: Lebanon, NH, January 11, 2005.
- (26) Mädler, L.; Roessler, A.; Pratsinis, S. E.; Sahn, T.; Gurlo, A.; Barsan, N.; Weimar, U. *Sens. Actuators, B* **2006**, *114*, 283.
- (27) Pratsinis, S. E.; Kim, K.-S. *J. Aerosol Sci.* **1989**, *20*, 101.
- (28) Friedlander, S. K.; Fernandez de la Mora, J.; Gokoglu, S. A. *J. Colloid Interface Sci.* **1988**, *125*, 351.
- (29) Tena-Zaera, R.; Martinez-Tomas, M. C.; Hassani, S.; Triboulet, R.; Munoz-Sanjose, V. *J. Cryst. Growth* **2004**, *270*, 711.
- (30) Wang, G. Z.; Wang, Y.; Yau, M. Y.; To, C. Y.; Deng, C. J.; Dickon, H. L. Ng. *Mater. Lett.* **2005**, *59*, 3870.
- (31) Garcia, J. F.; Sanchez, S.; Metz, R. *Oxid. Met.* **2008**, *69*, 317.
- (32) Müller, R.; Lipinski, W.; Steinfeld, A. *Appl. Therm. Eng.* **2008**, *28*, 524.
- (33) Ji, Y.; Sohn, H. Y.; Jang, H. D.; Wan, B.; Ring, T. A. *J. Am. Ceram. Soc.* **2007**, *90*, 3838.
- (34) Ji, Y. M. S. Thesis, University of Utah, Salt Lake City, UT, 2007.

JP9070955